

End-wall effects on the transition between Taylor vortices and spiral vortices

Sebastian Altmeyer¹, Christian Hoffmann¹, Matti Heise², Alexander Pinter¹, Manfred Lücke¹, and Gerd Pfister²

¹*Institut für Theoretische Physik, Universität des Saarlandes, D-66123 Saarbrücken, Germany*

²*Institut für Experimentelle und Angewandte Physik, Universität Kiel, D-24098 Kiel, Germany*

We present numerical simulations as well as experimental results concerning transitions between Taylor vortices and spiral vortices in the Taylor-Couette system with rigid, non-rotating end-walls in axial direction. As in the axial periodic case, these transitions are performed by wavy structures appearing via a secondary bifurcation out of Taylor vortices and spirals, respectively. But in the presence of rigid lids, *pure* spiral solutions do not occur but are substituted by primary bifurcating, stable wavy spiral structures (wSPI). Similarly to the periodic system, we found a transition from Taylor vortices to wSPI mediated by so called wavy Taylor vortices (wTVF) and, on the other hand, a transition from wSPI to TVF triggered by a propagating defect. We furthermore observed and investigated the primary bifurcation of wSPI out of basic Ekman flow.

PACS numbers: 47.20.Ky, 47.32.cf, 47.54.-r

Keywords: Taylor vortices, Spiral vortices, Wavy structures, Secondary bifurcations

I. INTRODUCTION

The interaction between Taylor vortex flow (TVF), spirals (SPI), and a variety of different wavy solutions was investigated in numerous publications [1, 2, 3, 4, 5, 6, 7, 8, 9].

Under periodic boundary conditions (pbc), toroidally closed TVF appears via a primary stationary bifurcation out of the rotationally symmetric, axially homogeneous basic circular Couette flow (CCF). Also the two axially symmetry degenerated, oscillatory SPI states appear via primary bifurcations out of CCF in a symmetric Hopf bifurcation together with the ribbon state. The latter is typically unstable close to onset and can be seen as a non-linear superposition of the two oppositely propagating spirals to an axially standing wave. The stability of TVF and SPI at onset is regulated by the order of their appearance upon increasing the inner cylinder's rotation rate: the first (second) solution to bifurcate out of CCF is stable (unstable). However, the second unstable solution becomes stable at larger inner cylinder rotation. Which state bifurcates first depends on the outer cylinder rotation rate [10].

Besides parameter regions with mono-stability of TVF and SPI, one also observes regions with bistability of both

states [11]. When moving a control parameter out of this region, one solution loses its stability and the flow undergoes a transition to the remaining stable state, i.e., from TVF to SPI or vice versa [11]. Bifurcation theoretical considerations and symmetry arguments [1, 2] as well as amplitude expansion techniques in [3] and numerical simulations in [9] show that the stability is transferred from TVF to SPI via secondarily bifurcating wavy Taylor vortices (wTVF) [3, 4] and vice versa from SPI to TVF via secondarily bifurcating wavy spirals (wSPI). The solution branch of stable TVF (SPI) is connected to unstable ribbons [12] via stable wTVF (wSPI). Then, a 'jump' bifurcation [1] from the end of the stable wTVF (wSPI) branch leads to the stable SPI (TVF) branch. This bifurcation behavior is schematically illustrated in Fig. 1.

Note that in the majority of publications, the wTVF solution branch has been seen to return to the TVF branch or to undergo higher order bifurcations [4, 6, 7, 8, 13, 14] at larger driving.

On the other hand, rigid non-rotating lids at the axial ends (rigid boundary conditions, rbc) induce rotational symmetric Ekman vortices even for sub-critical driving [10]. This modifies the structure, stability and bifurcation behavior of the different states.

One important difference between pbc and rbc is the absence of *pure* SPI solutions for rbc, in particular, for moderate outer cylinder rotation, i.e. within the left part of Fig. 1. The rotational-symmetric Ekman modes interact with the spiral modes leading to wSPI which bifurcate primarily out of the basic Ekman state and play a similar role as the SPI under pbc [9].

Furthermore, under rbc, wSPI loses its stability for stronger inner cylinder rotation and we found traveling defects which trigger the transition from wSPI to stable TVF.

In [15], we described a situation where a similar defect which separates domains of oppositely traveling spiral waves propagates through the system and trigger a transition from right-handed to left-handed spirals or vice

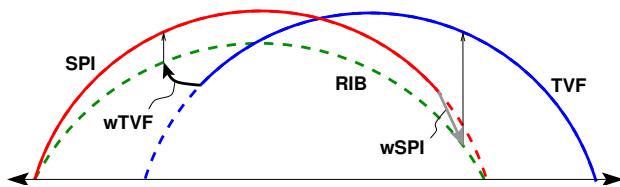


FIG. 1: (Color online) Schematic bifurcation diagram for a suitably chosen control parameter. Stable (unstable) solutions are displayed as solid (dashed) lines. Thin arrows indicate the transients corresponding to the 'jump' bifurcation mentioned in [1].

versa. Thus, the transition from wSPI to TVF is a further example for a transition which is triggered by a propagating defect.

This paper elucidates how TVF are transformed into SPI and vice versa under the presence of Ekman induced disturbances, how stability is transferred between the branches, and where and what kind of transients occur under rbc. It is roughly divided into two parts corresponding to the transition from TVF to wSPI via wTVF and the transition from wSPI to TVF via a propagating defect. Structural dynamics, frequencies and wave number selection are discussed and a comparison of the results obtained for rbc and pbc is made.

II. SYSTEM

The Taylor-Couette system consists of a fluid of kinematic viscosity ν in the gap between two concentric, independently rotating cylinders (inner, outer radius $r_{1,2}$; angular velocities $\Omega_{1,2}$; fixed radius ratio $\eta = r_1/r_2 = 0.5$ and fixed length $\Gamma = 12$ in units of the gap width $d = r_2 - r_1$) and non-rotating, rigid lids at the axial ends.

Cylindrical coordinates r, φ, z are used to decompose the velocity field into a radial component u , an azimuthal one v , and an axial one w

$$\mathbf{u} = u \mathbf{e}_r + v \mathbf{e}_\varphi + w \mathbf{e}_z. \quad (2.1)$$

The system is governed by the Navier-Stokes equations

$$\partial_t \mathbf{u} = \nabla^2 \mathbf{u} - (\mathbf{u} \cdot \nabla) \mathbf{u} - \nabla p. \quad (2.2)$$

Here, lengths are scaled by the gap width d and times by the radial diffusion time d^2/ν for momentum across the gap and the pressure p by $\rho\nu^2/d^2$. The Reynolds numbers

$$R_1 = r_1 \Omega_1 d / \nu, \quad R_2 = r_2 \Omega_2 d / \nu \quad (2.3)$$

enter into the boundary conditions for v . R_1 and R_2 are just the reduced azimuthal velocities of the fluid at the cylinder surfaces. Within this paper, we hold fixed $R_2 = -100$.

For numerical simulations, we used the G1D3 code described in [11, 16], i.e. a combination of a finite differences method in radial r and axial z direction and a Galerkin expansion in φ direction:

$$f(r, \varphi, z, t) = \sum_m f_m(r, z, t) e^{im\varphi}, \quad (2.4)$$

$$f \in \{u, v, w, p\}$$

In the experimental setup, the inner cylinder ($r_i = 12.50 \pm 0.01$ mm) is machined from stainless steel, while the outer cylinder ($r_o = 25.00 \pm 0.01$ mm) is made from optically polished glass. As fluid thermostatically controlled silicone oil with a kinematic viscosity $\nu = 10.6$ cS

is used. At top and bottom the flow is confined by massive end-walls with a till better than 0.03 mm at the outer diameter. The flow is visualized by elliptical aluminum particles having a length of 80 μm . Flow visualization measurements are performed by monitoring the system with a CCD-camera in front of the cylinder recording the luminosity along a narrow axial stripe. The spatio-temporal behavior of the flow is then represented by successive stripes for each time step at a constant φ position leading to continuous space time plots.

III. TRANSITIONS BETWEEN TVF AND WSPI

As in the periodic system [9], we also found transitions between the two primary bifurcating structures TVF and (w)SPI in the finite length system. The main difference between both is that we do not observe (neither in simulations nor in experiments) *pure* spirals for $\Gamma = 12$ systems, i.e. helical structures with the continuous symmetry given by $f(r, \varphi, z, t) = f(r, kz + M\varphi - \omega t)$ for fixed M , k , and ω (c.f. [11]). In finite systems with non-rotating lids generating Ekman vortices with an exponentially decaying amplitude in axial direction, pure SPI are replaced by wSPI with a more complex mode spectrum as described in [9]. This is due to the interaction between the spiral and the Ekman modes. This section describes first the bifurcation from TVF to wSPI via wTVF and after that the transition from wSPI to TVF.

A. Bifurcation from TVF to wSPI

Fig. 2 depicts the bifurcation branches for the interesting states (w)SPI, (w)TVF, and ribbons. The different structures are distinguished by symbols and line colors and characterized by amplitudes and frequencies of their significant Fourier modes (m, k) determined by the azimuthal wave number m and the axial wave number k of the complete structure. The latter is included in the legend box. Solid (dashed) lines with filled (open) symbols represent stable (unstable) solutions. Fig. 2(a) and (b) present mode amplitudes $|u_{m,k}|$ of the radial velocity field u in the finite case (a) and the periodic case (b), respectively. (c) and (d) show the corresponding frequencies $|\omega_{m,k}|$.

With our way of characterizing the flow by the combination of azimuthal and axial Fourier modes, with the latter being obtained over the full axial extension of the system, we do not capture, e.g. the Ekman induced axial variation of $m = 0$ modes.

We start our discussion of the bifurcation diagram in Fig. 2(a) in region E' with a stable $k = 4.85$ TVF state which loses its stability in region F' and C'. This is exactly the same behavior as under pbc (b), except that the stability thresholds are slightly shifted, that the unstable TVF branch bifurcates out of the $k = 3.95$ Ekman state in (a) instead of the CCF as in (b), and - more

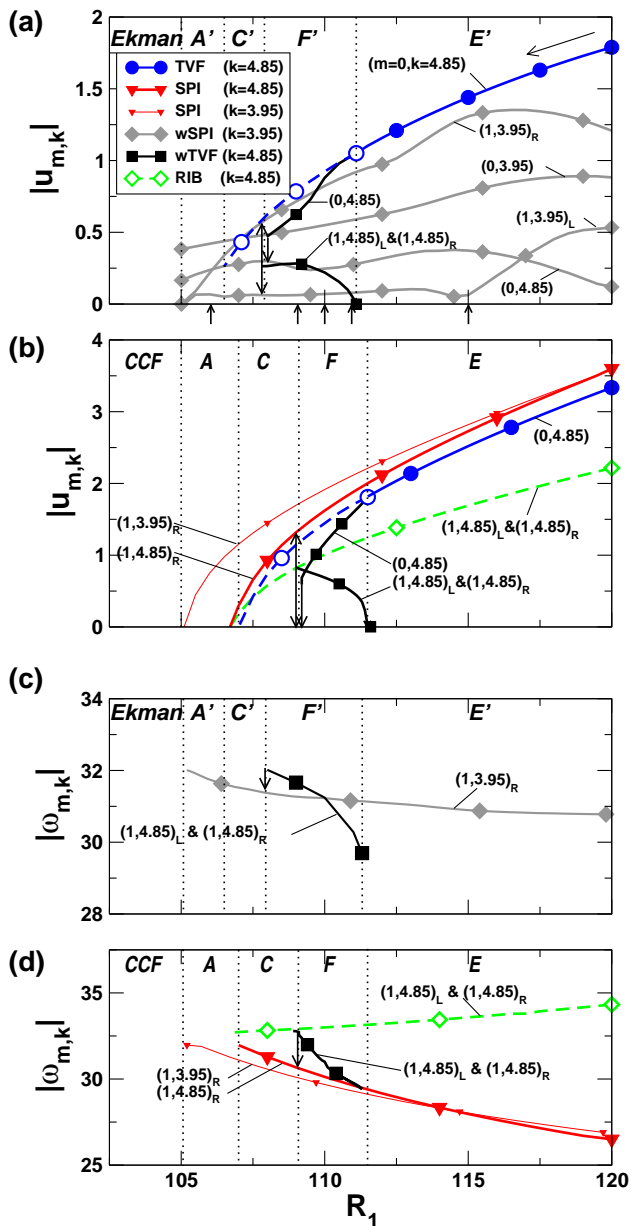


FIG. 2: (Color online) Numerically obtained bifurcation diagrams for different vortex structures TVF (blue, circles), SPI (red, triangles), wTVF (black, squares), wSPI (gray, diamonds), and ribbons (RIB, green, diamonds) versus R_1 for rbc (a,c) as well as for pbc (b,d). Curves with the same color, symbol, and line-width represent different modes of the same solution. Solid (dashed) lines with filled (open) symbols refer to stable (unstable) states. Shown are the significant radial flow field amplitude modes $|u_{m,k}|$ at mid-gap (a,b) and the corresponding frequencies $|\omega_{m,k}|$ (c,d). The indices R and L correspond to right- and left-handed spiral modes. The short arrows pointing to the abscissa in (a) denote the R_1 values of the snapshots in Fig. 3, the long arrow in (a) indicates the direction for the transition TVF \rightarrow wTVF \rightarrow wSPI. The sections labelled with letters correspond to different stability regions as listed in the table (c.f. Fig. 3 in [9]):

region	A	A'	C	C'	F	F'	E	E'
TVF	-	-	u	u	u	u	s	s
SPI	s	-	s	-	s	-	s	-
wSPI	-	s	-	s	-	s	-	s
wTVF	-	-	-	-	s	s	-	-
RIB	u	-	u	-	u	-	u	-

stable (s)
 unstable (u)
 nonexistent (-)

importantly – that the final state is a wSPI and not a pure SPI. We omit the Ekman branch itself in the figure due to visibility reasons.

In F' (and also in F), TVF becomes unstable against wTVF maintaining the same wave number ($k = 4.85$). Note that in (b), the wave number is determined by the predefined periodicity length. At the right border of C (C'), wTVF undergoes a transition to the remaining stable SPI (wSPI) solution with $k = 4.85$ ($k = 3.95$), i.e., the wave number changes during this transition – c.f. [9] for a detailed description of the stability properties, the bifurcation behavior, and the structure of wTVF and wSPI.

We added the corresponding $k = 3.95$ SPI solution branch in (b) in order to emphasize the identical onsets of $k = 3.95$ SPI (b) and $k = 3.95$ wSPI (a). As the SPI solution in (b), also the wSPI solution in (a) is stable within the whole parameter range displayed here. The transition from wTVF to SPI (wSPI) includes an unstable transient ribbon state, but we did not try to stabilize this state for rbc.

Generally speaking, there are three major aspects concerning the finite and the periodic system: (i) wSPI in (a) play quite the same role as the pure SPI in (b) – we indicated this by the prime at the labels A,C,E,F distinguishing the different stability regions (c.f. [9, 17]). (ii) for transition TVF \rightarrow wSPI, the finite $\Gamma = 12$ system selects the same wave number $k = 4.85$ for *all* toroidally closed structures (TVF, wTVF) and $k = 3.95$ for the helical solution (wSPI). Thus, transitions from TVF to wSPI are generally accompanied by a change in the wave number. (iii) finite boundary conditions superimpose rotational symmetric disturbances. Therefore, all thresholds (dotted vertical lines in Fig. 2(a,b)) of solutions with rotational or toroidal symmetry are shifted towards lower R_1 compared to the respective thresholds in the periodic system. The wTVF onsets E-F and E'-F' coincide very well in both cases.

In Fig. 2(a), the dominant mode (0, 4.85) of the unstable $k = 4.85$ TVF branch ends up in the (0, 4.85) Ekman mode at A'-C' which is a sub-dominant mode in the $k = 3.95$ Ekman state. Therefore, we included the mode (0, 4.85) which is a higher Fourier mode of the $k = 3.95$ wSPI state.

Note that due to the absence of symmetry breaking effects like axial through-flow, right-handed and left-handed spiral solutions are equivalent [11, 17] and therefore simply indicated by (w)SPI.

1. Frequencies

Fig. 2(c) and (d) provide the frequencies $|\omega_{m,k}|$ of the corresponding mode amplitudes in (a) and (b). We omit those frequencies of TVF and wTVF which are zero.

SPI – for pbc (d), spirals and ribbons grow via a primary Hopf bifurcation with a common frequency out of CCF. The difference between the spiral frequencies for pbc (d) and rbc (c) is a consequence of the Reynolds-

stress driven (intrinsic) axial net flow which is directed oppositely to the spiral propagation. In finite systems, this net flow is suppressed by impermeable lids which leads to a shift in the axial phase velocity and thereby also in the frequency [11]. This effect can also be seen for the wSPI in (c) and the SPI in (d): whereas the frequencies of both spirals ($k = 4.85$ and $k = 3.95$) are nearly identical at E-F, the frequencies of the $k = 3.95$ SPI at E-F and the $k = 3.95$ wSPI at E'-F' differ.

wTVF – On the other hand, the wTVF frequencies at the bifurcation thresholds E-F and E'-F' are almost identical. Here, the intrinsic net flow of the $(1, 4.85)_L$ mode is compensated by that of the $(1, 4.85)_R$ mode in both cases (c) and (d). Moreover, the variation of wTVF and SPI frequencies in region F differs significantly.

Since wTVF is a time-periodic rotating state that does not propagate axially, all mode frequencies are either zero ($\omega_{0,4.85} = 0$) or multiples of $\omega_{1,4.85}$. So, the dynamics of wTVF is rather simple while the spatial structure is more complex.

2. Spatio-temporal behavior

In order to elucidate the different states arising during the transition TVF (snapshot #5) \rightarrow wTVF (#4, #3) \rightarrow wSPI (#2, #1), Fig. 3(a) gives isosurfaces of the azimuthal vorticity $\partial_z u - \partial_r w$ of stationary states at different R_1 values which are marked by short arrows pointing to the abscissa of Fig. 2(a).

The pure $k = 4.85$ TVF state (#5) becomes unstable against toroidally closed but axially modulated $k = 4.85$ wTVF (#4). Obviously, the modulation strength increases towards mid-system where the Ekman influence is minimal. As the $m \neq 0$ mode contributions grow, the formerly rotational symmetric structure becomes more and more deformed and the vorticity tubes narrow at a certain φ position (#4). This means that the maximal vorticity within the (r, z) plane at this φ position decreases with R_1 – the vortex 'intensity' becomes weaker there. Note that this indentation of the vortex tubes as well as the defect rotate with the whole structure.

Finally, the isosurfaces are completely constricted and separated (#3). After displacing the ends of the tubes, new connections are established and the vorticity increases now to the final distribution in the $k = 3.95$ wSPI (#2).

The last snapshot, (#1), depicts a situation in which the system is very weakly supercritical and therefore, the Ekman vortices remain the dominant structure.

Fig. 3(b) presents the experimentally obtained spatio-temporal behavior describing the dynamics of the different states after an initial jump from $R_1 = 115$ to 109 at the right border of the plot beginning with a pure TVF state in (#5) with $k \approx 4.8$ which then undergoes (beginning at mid-height) a transition to wTVF with the same axial wave number (#4). After a transient (#3) which corresponds to the 'jump' bifurcation described above,

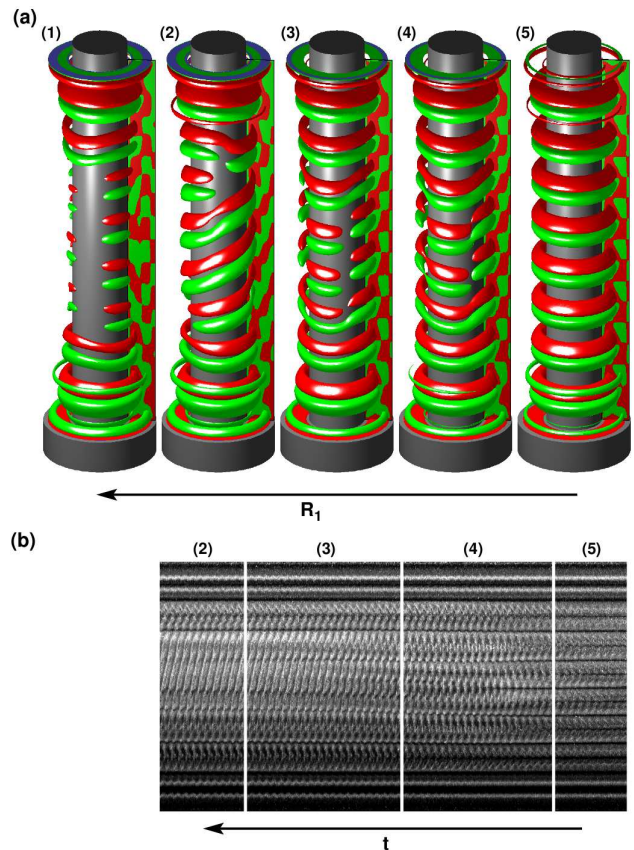


FIG. 3: (Color online) (a) Numerical simulations: snapshots of isosurfaces of the azimuthal vorticity $\partial_z u - \partial_r w = \pm 40$ (red: +40, green: -40) at five different R_1 values marked by arrows in Fig. 2(a) during the transition TVF \rightarrow wTVF \rightarrow wSPI (from right to left). Red (green) coloring on the additional $\varphi = \text{const.}$ plane denotes positive (negative) vorticity. We use 4π cylinders in (a) in order to present the whole structure in one single 3-dimensional plot. (b) Experimentally obtained spatio-temporal flow visualization of the transition which was triggered by an initial jump from $R_1 = 115$ to 109. The plots cover the complete system length of $\Gamma = 12$.

wSPI with $k = 3.6$ are finally established (#2). Note that we also verified in further experiments the stability and stationarity of the TVF (#5), wTVF (#4), and wSPI (#2) states for suitable fixed control parameters R_1 .

3. Wave number selection

Due to the finite boundary conditions, the toroidally closed structures (TVF, wTVF) can occur with discretely different axial wave numbers depending on the initial conditions. We found at least three stable TVF states with 7 ($k = 3.83$), 8 ($k = 4.85$), and 9 ($k = 5.81$) vortex pairs in region E' (only the 8 vortex pairs TVF state is

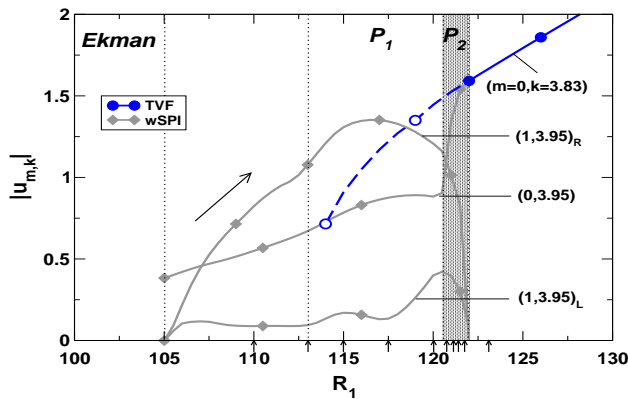


FIG. 4: (Color online) Extension of Fig. 2(a) – see description there. Short arrows pointing to the abscissa identify the snapshots in Fig. 5(a). The long arrow indicates the direction of the transition wSPI \rightarrow TVF.

presented in Fig. 2 and 3). All of them undergo a transition to wTVF in region F' for specific R_1 values without changing their respective wave number k . Finally, all wTVF states 'jump' (accompanied by a change in k) to the $k = 3.95$ wSPI solution.

The experimentally ($k = 4.53$ for (w)TVF and $k = 4.03$ for wSPI) and the numerically ($k = 4.85$ for (w)TVF and $k = 3.95$ for wSPI) obtained axial wave numbers differ slightly. However, numerical simulations as well as experimental results exhibit the same jumps in k during the transition wTVF \rightarrow wSPI.

B. Transition from wSPI to TVF

Under pbc, one finds the bifurcation sequence SPI \rightarrow wSPI \rightarrow TVF. While the transition from wSPI to TVF is mediated by a 'jump' bifurcation [1, 9], pure SPI, on the other hand, could not be observed neither in rbc simulations nor in experiments.

As described above for rbc, wSPI bifurcates primarily out of the basic Ekman flow as a stable solution for stronger counter-rotation. However, we found wSPI to become unstable against TVF via an other kind of transition taking place beyond region E' of Fig. 2(a). This transition is mediated by a propagating defect which separates the wSPI from a wTVF regime pushing wSPI out and pulling wTVF through the bulk. Once the defect crossed the whole bulk, the modulation amplitude of the wTVF vanishes and pure TVF remains.

Fig. 4 gives an enhanced version of the bifurcation diagram in Fig. 2(a) with a slightly extended R_1 range covering the transient wSPI \rightarrow TVF transition in the gray marked region P₂. The short arrows mark the R_1 values for which isovorticity snapshots are presented in Fig. 5(a).

Starting with a pure wSPI solution at small R_1 , an additional defect is generated near the upper Ekman-spiral

defect after increasing R_1 beyond the left border of region P₁ and remains at its axial position for any R_1 within the whole region P₁. At the right border of P₁, the defect begins to propagate towards the other axial end. This is a transient state which ends up in a pure $k = 3.83$ TVF solution after the annihilation of the propagating spiral-spiral defect at the lower Ekman-spiral defect. The gray marked region P₂ gives the behavior of the amplitudes during this transient from wSPI to TVF which occurs within the range $120 < R_1 < 122$. Note that the final TVF ($k = 3.83$) is different from that discussed in Fig. 2(a) which has $k = 4.85$. This TVF state is one of several stable TVF states with different wave numbers (c.f. Sec. III A 3).

This transition sequence agrees with experimental results as presented in Fig. 5(b) showing a spatio-temporal flow visualization of the transition even after an initial jump from $R_1 = 107$ to 120 at the left border of the plot.

1. Spatio-temporal behavior

The arrows in Fig. 4 mark the R_1 values of the ten snapshots of Fig. 5 depicting the isosurfaces of the azimuthal vorticity (a) as well as a spatio-temporal plot of the experimentally obtained velocity field (b). Both sequences illustrate the structural changes during the transition wSPI \rightarrow TVF mediated by a propagating defect.

Starting with a wSPI state (#1) in Fig. 5 and increasing R_1 , the second upper closed vortex becomes wavy-like deformed in axial direction (#2-#5) while the deformation rotates with the whole structure. The modulation becomes stronger with increasing R_1 until a second defect evolves out of the phase generating Ekman spiral defect (#2).

In (#5), this defect detaches from the upper Ekman vortex and begins to propagate (#6)-(#9), pushing the wSPI and pulling a wTVF state through the bulk. Therefore, the localized wSPI region shrinks and the localized wTVF domain grows. During this process, neither the wave number of wSPI nor that of wTVF change significantly, because new wTVF vortices are generated directly behind the propagating defect: comparing (#7) and (#8), one observes that the vortex tubes become constricted and separated and after displacing the ends of the tubes, new connections are established and a new wTVF vortex is generated. Finally, the defect reaches the bottom end and merges with the lower Ekman vortex (#10) leaving behind a pure TVF state.

As described above, Fig. 5(b) elucidates the spatio-temporal behavior during the transition after an initial jump from $R_1 = 107$ to 120 at the left border of the plot. As in the numerical simulations, the experimental setup realizes a transition from wSPI to TVF via a propagating defect. Furthermore, the experimental wave numbers for wSPI $k = 4.03$ and TVF $k = 3.84$ agree very well with the numerical wave numbers for wSPI $k = 3.95$ and TVF $k = 3.83$.

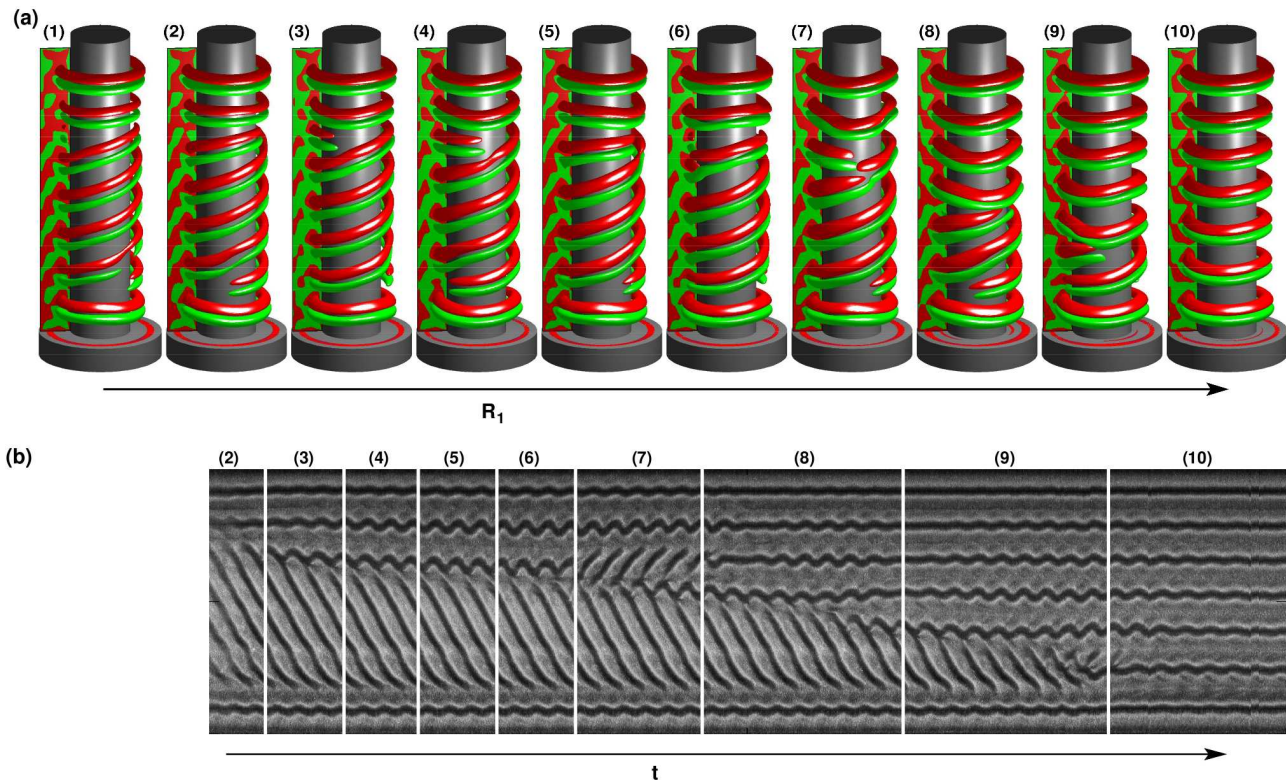


FIG. 5: (Color online) (a) Numerical simulations: snapshots of isosurfaces of the azimuthal vorticity $\partial_z u - \partial_r w = \pm 40$ (red: +40, green: -40) of flow states at ten different R_1 values marked by short arrows pointing to the abscissa in Fig. 4 and visualizing the transition wSPI \rightarrow TVF while increasing R_1 . Red (green) coloring on the additional $\varphi = \text{const.}$ planes denote positive (negative) vorticity. 4π cylinders are used in order to present the whole structure in one single 3-dimensional plot. Note that the propagating defect (#5-#9) is a transient state. (b) Experimentally obtained spatio-temporal flow visualization of the transition which was triggered by an initial jump from $R_1 = 107$ to 120. In axial direction, the plots cover the complete system length of $\Gamma = 12$.

We'd like to stress that in the here presented experiments, the transitions are initiated by an instantaneous jump (after preparing the initial state) into the parameter regime where the final structure was expected to be stable. The experimentally obtained spatio-temporal plots disclose a sequence of transient structures which correspond to stationary structures when quasi-statically driving the system by a R_1 ramp. We indicated the corresponding structures by identical numbers of the snapshots in Fig. 3 and 5.

IV. SUMMARY

We investigated the bifurcation behavior for the transition between Taylor vortices and wavy spirals in a finite length Taylor-Couette system with non-rotating, rigid lids. In contrast to periodic boundary conditions where *pure* SPI solutions exist (even for outer cylinder at rest), here, helical solutions occur as wavy structures due to the admixture of Ekman induced $m = 0$ mode components in the Fourier spectra.

Under finite system geometry, we found a transition

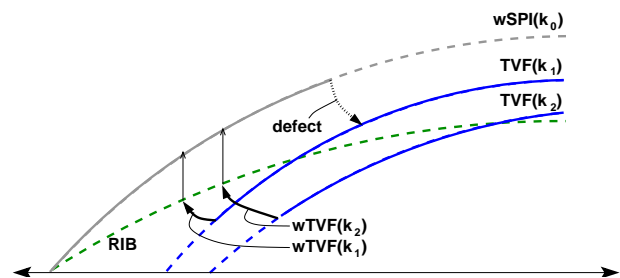


FIG. 6: Schematic bifurcation diagram for a suitable chosen control parameter containing the results of Fig. 2(a) and Fig. 4 for the finite system (in contrast to Fig. 1 for the periodic system). Stable (unstable) solutions are displayed as solid (dashed) lines. Thin arrows indicate the transients corresponding to the 'jump' bifurcation. We included the ribbon branch as an intermediate unstable solution.

from TVF to wSPI via wTVF which is analogue to the transition from TVF to SPI via wTVF in the periodic system. wSPI (helical open vortices) are selected with a distinct wave number k_0 whereas several bi-

furcation branches corresponding to TVF and wTVF states (toroidally closed vortices) exist simultaneously and multi-stably with different axial wave numbers (e.g. k_1 and k_2), i.e. different numbers of vortex pairs (as schematically depicted in Fig. 6). The transitions from TVF to wSPI and vice versa are in general accompanied by a change in k .

An other kind of transition performing the change from wSPI to TVF is triggered via a propagating defect. This defect pushes the wSPI out of the system and pulls wTVF and finally TVF into the bulk.

The coincidence of the wTVF frequency and the SPI frequency at the bifurcation point disappears in the finite system.

Acknowledgement

We thank the Deutsche Forschungsgemeinschaft for support.

-
- [1] M. Golubitsky, I. Stewart, and D. Schaeffer, *Singularities and Groups in Bifurcation Theory II* (Springer, New York, 1988), pp. 485–512.
 - [2] M. Golubitsky and W. F. Langford, *Physica D* **32**, 362 (1988).
 - [3] G. Iooss, *J. Fluid Mech.* **173**, 273 (1986).
 - [4] C. A. Jones, *J. Fluid Mech.* **157**, 135 (1984).
 - [5] R. Tagg, D. Hirst, and H.L. Swinney, Experiments cited in [2] (as '[1988]' on p. 508), unpublished.
 - [6] C. D. Andereck, S. S. Lui, and H. L. Swinney, *J. Fluid Mech.* **164**, 155 (1986).
 - [7] J. Antonijoan and J. Sanchez, *Phys. Fluids* **12**, 3147 (2000).
 - [8] J. Antonijoan and J. Sanchez, *Phys. Fluids* **14**, 1661 (2002).
 - [9] Ch. Hoffmann, S. Altmeyer, and M. Lücke, *New J. Phys.* **11**, 053002 (2009).
 - [10] R. Tagg, *Nonlinear Science Today* **4**, 1 (1994).
 - [11] Ch. Hoffmann, M. Lücke, and A. Pinter, *Phys. Rev. E* **69**, 056309 (2004).
 - [12] P. Chossat and G. Iooss, *The Couette-Taylor Problem* (Springer-Verlag, New York, 1994).
 - [13] G. Ahlers, D. S. Cannell, and M. A. Dominguez Lerma, *Phys. Rev. A* **27**, 1225 (1983).
 - [14] K. Park, *Phys. Rev. A* **29**, 3458 (1984).
 - [15] M. Heise, Ch. Hoffmann et al, *Phys. Rev. Lett.* **100**, 064501 (2008).
 - [16] Ch. Hoffmann and M. Lücke, in *Physics of rotating fluids* (Springer Verlag, Berlin, 2000), pp. 55–66.
 - [17] Ch. Hoffmann, M. Lücke, and A. Pinter, *Phys. Rev. E* **72**, 056311 (2005).